

ARCHITECTURAL CO-DESIGN FOR ZERO-SHOT ANOMALY DETECTION: DECOUPLING REPRESENTATION AND DYNAMICALLY FUSING FEATURES IN CLIP

Ke Ma¹ Jun Long¹ Hongxiao Fei¹ Liujie Hua¹ Yiran Qian¹ Zhen Dai² Yueyi Luo^{1*}

¹Central South University, Changsha, China

²Hunan Vocational College of Science and Technology, Changsha, China

ABSTRACT

Pre-trained Vision-Language Models (VLMs) face a significant adaptation gap when applied to Zero-Shot Anomaly Detection (ZSAD), stemming from their lack of local inductive biases for dense prediction and their reliance on inflexible feature fusion paradigms. We address these limitations through an Architectural Co-Design framework that jointly refines feature representation and cross-modal fusion. Our method proposes a parameter-efficient **Convolutional Low-Rank Adaptation** (Conv-LoRA) adapter to inject local inductive biases for fine-grained representation, and introduces a **Dynamic Fusion Gateway** (DFG) that leverages visual context to adaptively modulate text prompts, enabling a powerful bidirectional fusion. Extensive experiments on diverse industrial and medical benchmarks demonstrate superior accuracy and robustness, validating that this synergistic co-design is critical for robustly adapting foundation models to dense perception tasks.

Index Terms— anomaly detection, multimodal feature fusion, vision-language model, transfer learning, PEFT

1. INTRODUCTION

Zero-Shot Anomaly Detection (ZSAD) leverages Vision-Language Models (VLMs) [1, 2] like CLIP [3] to bypass the need for extensive, category-specific training data required by traditional methods [4, 5]. The dominant paradigm adapts these VLMs via text prompts, which has evolved from hand-crafted ensembles (e.g., WinCLIP [6]) to learnable prompts tuned on auxiliary data. These advanced methods explore object-agnostic semantics (AnomalyCLIP [7]), dynamic prompt generation (AdaCLIP [8]), and multi-layer feature queries (CLIP-AD [9]). However, this line of work faces two fundamental limitations.

First, these methods rely on an **inflexible fusion paradigm** [Figure 1(a)], treating the VLM’s architecture as a fixed black box. This static, layer-wise alignment assumes a fixed semantic correspondence that often fails to capture the diverse nature of anomalies. Second, a deeper **representational adaptation gap** exists, as CLIP’s Vision Transformer (ViT) [10] architecture lacks the local inductive biases inherent in CNNs [11, 12], which are critical for fine-grained spatial tasks.

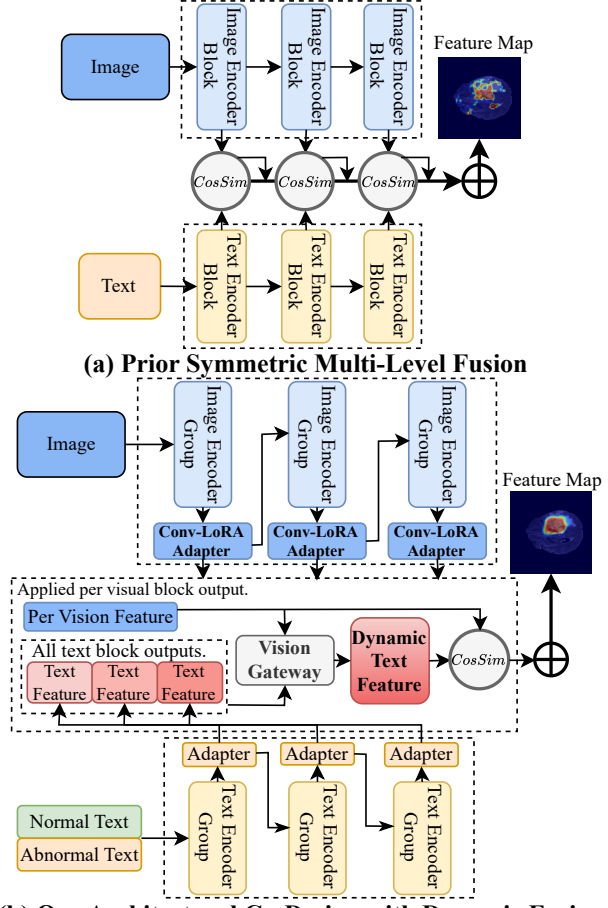


Fig. 1. Comparison of fusion paradigms. (a) Prior works rely on a rigid, static alignment between corresponding feature blocks. (b) Our Architectural Co-Design enables a flexible fusion policy by enriching visual features with local priors (Conv-LoRA) and then dynamically generating tailored text descriptors for each visual level (DFG).

To address these core issues, we introduce the Architectural Co-Design CLIP (ACD-CLIP) framework [Figure 1(b)], a novel approach that synergistically refines both feature representation and cross-modal fusion. The synergy is crucial: the Conv-LoRA adapter provides fine-grained details that are fully exploited by the DFG’s adaptive fusion mechanism. Our architectural modifications are enabled by Parameter-Efficient Fine-Tuning (PEFT) [13, 14]. While recent works

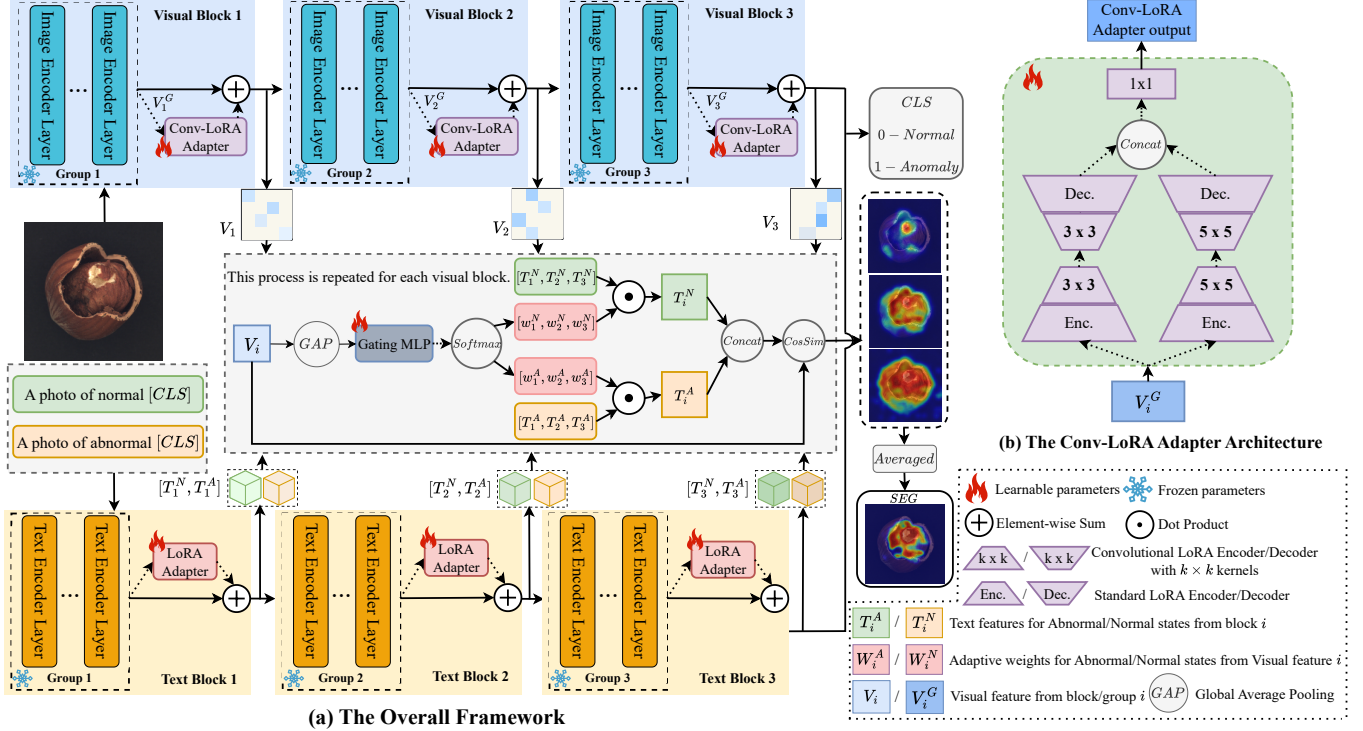


Fig. 2. Overview of the proposed ACD-CLIP architecture. (a) The Overall Framework: We structure CLIP’s vision and text encoders into a hierarchy of N sequential **Groups** (as illustrated, $N = 3$). Each vision group is enhanced by a trainable **Conv-LoRA Adapter** to instill local priors, while each corresponding text group incorporates a standard LoRA adapter. The **Dynamic Fusion Gateway (DFG)** then uses each visual feature V_i to generate a tailored text descriptor for producing a level-specific anomaly map. **(b) The Conv-LoRA Adapter:** Our parameter-efficient adapter features a multi-branch design with multi-scale convolutions inside a LoRA bottleneck.

have shown the value of integrating convolutional structures into PEFT adapters for general vision tasks [15, 16], our work is the first to co-design such an adapter with a dynamic fusion mechanism specifically for ZSAD. Our contributions are: 1) A parameter-efficient **Conv-LoRA Adapter** to inject local inductive biases for fine-grained representation. 2) A **Dynamic Fusion Gateway (DFG)**, a vision-guided mechanism enabling a flexible, bidirectional fusion policy. 3) Validation of our method, which yields **significant performance gains** on diverse industrial and medical ZSAD benchmarks.

2. METHODOLOGY

As illustrated in Figure 2, our ACD-CLIP framework introduces two core innovations to adapt VLMs for ZSAD: (1) an architectural co-design for decoupled representation learning, and (2) a dynamic gateway for cross-modal fusion.

2.1. Hierarchical Feature Adaptation with Local Priors

To mitigate feature entanglement, we partition the vision and text encoders into N sequential **Groups**, encouraging each to specialize in representations at a distinct semantic level. To instill local inductive priors, we integrate a parameter-efficient **Conv-LoRA Adapter** into each vision group. The adapter processes the sequential output from a ViT block, $X_{\text{in}} \in \mathbb{R}^{B \times L \times C}$.

The adapter features a parallel multi-branch design with distinct $k \times k$ convolutional kernels (where $k \in \{3, 5\}$) that operate within a LoRA-style bottleneck. This structure allows it to capture local patterns at varied receptive fields while maintaining parameter efficiency. The entire operation, Φ_{Adapter} , generates a residual update ΔX by fusing the outputs of the parallel branches:

$$\begin{aligned} \Delta X &= \Phi_{\text{Adapter}}(X_{\text{in}}) \\ &= \mathcal{R}_{\text{seq}} \left(\text{Conv}_{1 \times 1} \left(\mathcal{R}_{2\text{D}} \left(\text{Concat} \left[X_{\text{branch.out}}^{(k)} \right] \right) \right) \right) \quad (1) \end{aligned}$$

The output of each branch, $X_{\text{branch.out}}^{(k)}$, is generated in a two-step process. First, the input tensor X_{in} is projected to a low-rank space by W_{down} , reshaped, and passed through a $k \times k$ convolution to instill local context and transform the features, producing an intermediate feature map $X_{\text{conv}}^{(k)}$:

$$X_{\text{conv}}^{(k)} = \frac{1}{k} \text{Conv}_{\text{down}}^{(k)} \left(\mathcal{R}_{2\text{D}}(X_{\text{in}} W_{\text{down}}) \right) \quad (2)$$

This feature map is then processed by a second $k \times k$ convolution for further feature refinement, reshaped back into a sequence, and projected up by W_{up} to yield the final branch output:

$$X_{\text{branch.out}}^{(k)} = \mathcal{R}_{\text{seq}} \left(\frac{1}{k} \text{Conv}_{\text{up}}^{(k)} \left(X_{\text{conv}}^{(k)} \right) \right) W_{\text{up}} \quad (3)$$

Here, W_{down} and W_{up} are the LoRA projection matrices performing channel-wise compression and expansion. $\mathcal{R}_{2\text{D}}$ and \mathcal{R}_{seq} are operators for reshaping between sequence and spatial formats. $\text{Conv}_{\text{up}}^{(k)}$ and $\text{Conv}_{\text{down}}^{(k)}$ are standard $k \times k$ convolutions that operate on feature channels for transformation and local context infusion while preserving spatial dimensions.

2.2. Dynamic Fusion Gateway

To overcome static fusion, our **Dynamic Fusion Gateway (DFG)** generates custom semantic descriptors for each visual feature group V_i . A global context vector $v_i^{\text{global}} = \text{GAP}(V_i)$ is extracted and passed through a gating MLP to produce logits l_i^s for each semantic state $s \in \{N, A\}$ (Normal, Abnormal). These logits determine the dynamic fusion weights $\omega_{i,j}^s$ for the set of all text features $\{T_j^s\}_{j=1}^N$:

$$\omega_{i,j}^s = \frac{\exp(l_{i,j}^s)}{\sum_{k=1}^N \exp(l_{i,k}^s)}, \quad \text{where } l_i^s = \text{MLP}_{\text{gate}}^s(v_i^{\text{global}}) \quad (4)$$

These weights dynamically fuse the multi-level text features to produce context-aware normal (T_i^N) and abnormal (T_i^A) descriptors:

$$T_i^s = \sum_{j=1}^N \omega_{i,j}^s \cdot T_j^s, \quad \text{for } s \in \{N, A\} \quad (5)$$

The resulting level-specific anomaly map, M_i , is then computed by applying a softmax function over the patch-wise cosine similarities between the visual features V_i and their corresponding dynamic text descriptors:

$$M_i = \frac{\exp(\text{sim}(V_i, T_i^A)/\tau)}{\exp(\text{sim}(V_i, T_i^N)/\tau) + \exp(\text{sim}(V_i, T_i^A)/\tau)} \quad (6)$$

where $\text{sim}(\cdot, \cdot)$ denotes the cosine similarity operator and τ is a temperature parameter. The final anomaly map is the average of these level-specific maps $\{M_i\}$.

2.3. Training Objective and Inference

The framework is trained end-to-end with a composite loss function, which jointly addresses pixel-level segmentation and image-level classification.

Segmentation Loss. The final prediction map is the average of level-specific maps, $M_{\text{seg}} = \frac{1}{N} \sum_{i=1}^N M_i$. It is optimized against the ground-truth mask M_{GT} using a combined Focal [17] and Dice loss [18]:

$$\begin{aligned} \mathcal{L}_{\text{seg}} = & \lambda_{\text{Focal}} \mathcal{L}_{\text{Focal}}(M_{\text{seg}}, M_{\text{GT}}) \\ & + \lambda_{\text{Dice}} \mathcal{L}_{\text{Dice}}(M_{\text{seg}}, M_{\text{GT}}) \end{aligned} \quad (7)$$

where λ_{Focal} and λ_{Dice} are balancing hyperparameters.

Classification Loss. For image-level classification, we compute the cosine similarity between the final global visual feature and the original, unfused text features from the last group, supervised via Cross-Entropy loss \mathcal{L}_{cls} . We use the original

text features here to provide a stable, high-level semantic anchor for the classification task.

Total Objective. The final training objective is a weighted sum of the two losses, balanced by the hyperparameter λ_{cls} :

$$\mathcal{L}_{\text{total}} = \mathcal{L}_{\text{seg}} + \lambda_{\text{cls}} \mathcal{L}_{\text{cls}} \quad (8)$$

Inference. A single forward pass generates the anomaly map M_{seg} and a classification score. The final image-level score combines the direct classification output with the maximum value from M_{seg} .

3. EXPERIMENTS

To demonstrate the efficacy and robustness of our ACD-CLIP framework, we conducted a comprehensive evaluation. This involved benchmarking our model against state-of-the-art (SOTA) competitors across a wide range of datasets and performing in-depth ablation studies to quantify the contribution of each individual component.

3.1. Experimental Setup

Datasets and Baselines. We perform a comprehensive evaluation on 12 public benchmarks spanning the industrial domain (MVTec-AD [19], VisA [20], BTAD [21], MPDD [22], RSDD [23]) and the medical domain (BrainMRI, Liver CT, and Retina OCT from BMAD [24], ColonDB [25], ClinicDB [26], Kvasir [27]). We benchmark against recent SOTA methods, including WinCLIP [6], CLIP-AD [9], AnomalyCLIP [7], and AdaCLIP [8].

Implementation Details. Our framework is built upon the pre-trained CLIP model with a ViT-L/14 backbone at a 336px resolution. To maintain a strict zero-shot setting, we train our model on an auxiliary dataset with no category overlap (VisA for all non-VisA benchmarks, and MVTec-AD for the VisA benchmark). We report the standard Area Under the Receiver Operating Characteristic curve (AUROC) and Average Precision (AP) for both pixel-level and image-level tasks.

3.2. Main Results and Analysis

As shown in Table 1, our ACD-CLIP framework consistently establishes a new state-of-the-art across both industrial and medical domains. On the widely-used MVTec-AD benchmark, our model excels at fine-grained localization, boosting pixel-level AP by nearly +10% over AnomalyCLIP. This superiority in capturing precise anomaly boundaries is a direct result of our architectural co-design.

Crucially, our approach shows strong cross-domain generalization. When trained solely on industrial data, ACD-CLIP excels on challenging medical benchmarks, achieving a pixel-level AUROC of 90.4% on ClinicDB and 96.6% on BrainMRI. Qualitative results (Figure 3) corroborate these gains, showing our model produces cleaner, more accurate anomaly maps with less noise.

Interestingly, our results across different numbers of groups (N) show that performance generally peaks around

Table 1. Quantitative comparison with state-of-the-art methods across diverse ZSAD benchmarks. Results are reported as (AUROC, AP) in percentage. **Blue:** Best result. **Red:** Second-best result.

Domain (Metric)	Dataset	WinCLIP	CLIP-AD	AnomalyCLIP	AdaCLIP	ours			
						<i>N</i> = 2	<i>N</i> = 3	<i>N</i> = 4	<i>N</i> = 6
Industrial (Pixel-level)	MVTec-AD	(85.1, 18.0)	(89.8, 40.0)	(91.1, 34.5)	(86.8, 38.1)	(91.7, 44.1)	(91.4, 43.6)	(90.9, 44.0)	(90.0, 43.1)
	BTAD	(71.4, 11.2)	(93.1, 46.7)	(93.3, 42.0)	(87.7, 36.6)	(96.3, 51.2)	(95.9, 51.2)	(96.5, 51.5)	(94.6, 51.1)
	MPDD	(95.2, 28.1)	(95.1, 28.4)	(96.2, 28.9)	(96.6, 29.1)	(97.0, 29.8)	(96.3, 30.3)	(96.1, 29.4)	(96.6, 30.3)
	RSDD	(95.1, 2.1)	(99.2, 31.9)	(99.1, 19.1)	(99.5, 38.2)	(99.1, 40.7)	(99.4, 41.3)	(98.9, 40.4)	(98.6, 40.1)
	VisA	(79.6, 5.0)	(95.0, 26.3)	(95.4, 21.3)	(95.1, 29.2)	(95.7, 27.8)	(95.9, 29.6)	(94.6, 27.5)	(94.1, 27.3)
Medical (Pixel-level)	ColonDB	(64.8, 14.3)	(80.3, 23.7)	(81.9, 31.3)	(79.3, 26.2)	(85.0, 35.9)	(85.1, 32.6)	(83.3, 35.4)	(80.7, 31.1)
	ClinicDB	(70.7, 19.4)	(85.8, 39.0)	(85.9, 42.2)	(84.3, 36.0)	(90.4, 53.5)	(89.2, 54.0)	(89.8, 56.1)	(85.0, 49.1)
	Kvasir	(69.8, 27.5)	(82.5, 46.2)	(81.8, 42.5)	(79.4, 43.8)	(88.5, 60.7)	(88.8, 60.2)	(88.8, 61.3)	(83.3, 54.8)
	BrainMRI	(86.0, 49.2)	(96.4, 54.2)	(95.6, 53.1)	(93.9, 52.3)	(96.6, 55.6)	(95.3, 53.0)	(97.0, 61.0)	(96.9, 56.1)
	Liver CT	(96.2, 7.2)	(95.4, 7.1)	(93.9, 5.7)	(94.5, 5.9)	(97.3, 8.8)	(97.2, 7.5)	(96.0, 6.8)	(95.3, 6.2)
Industrial (Image-level)	Retina OCT	(80.6, 39.8)	(90.9, 48.7)	(92.6, 55.3)	(88.5, 47.1)	(96.1, 66.2)	(93.7, 50.9)	(91.3, 48.2)	(91.5, 48.7)
	MVTec-AD	(89.3, 92.9)	(89.8, 95.3)	(90.3, 95.1)	(90.7, 95.2)	(90.9, 95.7)	(90.7, 95.8)	(92.4, 96.8)	(90.7, 95.7)
	BTAD	(83.3, 84.1)	(85.8, 85.2)	(89.1, 91.1)	(91.6, 92.4)	(93.5, 96.0)	(94.9, 98.0)	(93.3, 94.0)	(95.4, 98.2)
	MPDD	(63.6, 71.2)	(74.5, 77.9)	(73.7, 77.1)	(72.1, 76.9)	(78.1, 83.7)	(77.6, 82.3)	(74.7, 79.0)	(74.8, 78.2)
	RSDD	(85.3, 65.3)	(88.3, 73.9)	(73.5, 55.0)	(89.1, 70.8)	(94.0, 92.9)	(94.3, 92.7)	(93.4, 92.2)	(92.9, 91.9)
Medical (Image-level)	VisA	(78.1, 77.5)	(79.8, 84.3)	(82.1, 85.4)	(83.0, 84.9)	(85.6, 88.5)	(85.5, 88.1)	(83.0, 86.0)	(84.1, 86.7)
	BrainMRI	(82.0, 90.7)	(82.8, 85.5)	(86.1, 92.3)	(84.9, 94.2)	(89.1, 97.2)	(86.8, 96.9)	(88.1, 97.3)	(87.3, 97.1)
	Liver CT	(64.2, 55.9)	(62.7, 51.6)	(61.6, 53.1)	(64.2, 56.7)	(60.2, 54.2)	(65.8, 55.3)	(64.4, 57.3)	(68.4, 58.9)
Medical (Image-level)	Retina OCT	(42.5, 50.9)	(67.9, 71.3)	(75.7, 77.4)	(82.7, 80.3)	(84.4, 85.6)	(81.1, 80.9)	(80.3, 79.1)	(82.0, 79.7)

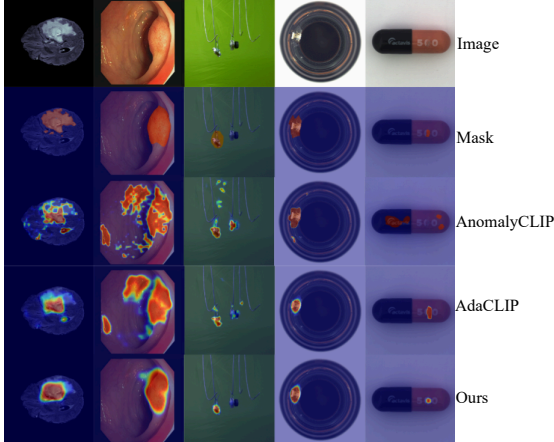


Fig. 3. Qualitative comparison on diverse industrial and medical datasets, showing our method’s superior localization accuracy and noise suppression over state-of-the-art baselines.

Table 2. Ablation study of our proposed components on the MVTec-AD dataset with a two-group configuration (*N* = 2). We report the average AUROC (%) for both pixel-level and image-level anomaly detection.

Configuration	Avg. AUROC	
	Pixel-Level	Image-Level
1. Baseline	82.3	81.2
2. + Conv-LoRA Adapter	89.1 (+6.8)	84.1 (+2.9)
3. + DFG	87.6 (+5.3)	85.9 (+4.7)
4. Ours (ACD-CLIP)	91.7	90.9

N = 3, suggesting a trade-off between hierarchical specialization and model complexity, where deeper partitioning does not necessarily yield further gains and may lead to overfitting on the auxiliary dataset.

3.3. Ablation Study

Our ablation study (Table 2) validates the individual and synergistic contributions of our two core components against a baseline using a standard LoRA adapter on ViT and static fusion. Integrating the **Conv-LoRA Adapter** alone boosts the pixel-level AUROC by 6.8%, confirming its critical role in providing the local inductive biases necessary for dense prediction. Separately, adding the **Dynamic Fusion Gateway (DFG)** improves the image-level AUROC by 4.7%, demonstrating the effectiveness of its vision-guided, adaptive fusion mechanism. The full ACD-CLIP model, which combines both, achieves the highest performance, confirming a powerful synergistic effect between enhancing feature representation and enabling dynamic cross-modal fusion.

4. CONCLUSION

In this work, we address the core limitations of Pre-trained Vision-Language Models for Zero-Shot Anomaly Detection by introducing a novel **Architectural Co-Design** framework. Our approach enhances both feature representation and cross-modal fusion: by injecting local inductive biases via a parameter-efficient **Conv-LoRA adapter** and replacing static alignment with a vision-guided **Dynamic Fusion Gateway**, our model learns fine-grained, context-aware features. This synergistic design achieves highly competitive results across diverse industrial and medical benchmarks, demonstrating substantial improvements in performance and stability. Ultimately, this work validates that a co-design of representation and fusion is a critical strategy for effectively adapting foundation models to dense perception tasks. We believe this principle can be extended to other domains such as zero-shot semantic segmentation and open-vocabulary detection.

5. REFERENCES

[1] Jean-Baptiste Alayrac, Jeff Donahue, Pauline Luc, Antoine Miech, Iain Barr, Yana Hasson, Karel Lenc, Arthur Mensch, Katherine Millican, Malcolm Reynolds, et al., “Flamingo: a visual language model for few-shot learning,” *Advances in neural information processing systems*, vol. 35, pp. 23716–23736, 2022.

[2] Haotian Liu, Chunyuan Li, Qingyang Wu, and Yong Jae Lee, “Visual instruction tuning,” *Advances in neural information processing systems*, vol. 36, pp. 34892–34916, 2023.

[3] Alec Radford, Jong Wook Kim, Chris Hallacy, Aditya Ramesh, Gabriel Goh, Sandhini Agarwal, Girish Sastry, Amanda Askell, Pamela Mishkin, Jack Clark, et al., “Learning transferable visual models from natural language supervision,” in *International conference on machine learning*. PMLR, 2021, pp. 8748–8763.

[4] Karsten Roth, Latha Pemula, Joaquin Zepeda, Bernhard Schölkopf, Thomas Brox, and Peter Gehler, “Towards total recall in industrial anomaly detection,” in *Proceedings of the IEEE/CVF conference on computer vision and pattern recognition*, 2022, pp. 14318–14328.

[5] Thomas Defard, Aleksandr Setkov, Angelique Loesch, and Romaric Audigier, “Padim: a patch distribution modeling framework for anomaly detection and localization,” in *International conference on pattern recognition*. Springer, 2021, pp. 475–489.

[6] Jongheon Jeong, Yang Zou, Taewan Kim, Dongqing Zhang, Avinash Ravichandran, and Onkar Dabeer, “Winclip: Zero-/few-shot anomaly classification and segmentation,” in *Proceedings of the IEEE/CVF Conference on Computer Vision and Pattern Recognition*, 2023, pp. 19606–19616.

[7] Qihang Zhou, Guansong Pang, Yu Tian, Shibo He, and Jiming Chen, “Anomalyclip: Object-agnostic prompt learning for zero-shot anomaly detection,” *arXiv preprint arXiv:2310.18961*, 2023.

[8] Yunkang Cao, Jiangning Zhang, Luca Frittoli, Yuqi Cheng, Weiming Shen, and Giacomo Boracchi, “Adaclip: Adapting clip with hybrid learnable prompts for zero-shot anomaly detection,” in *European Conference on Computer Vision*. Springer, 2024, pp. 55–72.

[9] Xuhai Chen, Jiangning Zhang, Guanzhong Tian, Haoyang He, Wuhan Zhang, Yabiao Wang, Chengjie Wang, and Yong Liu, “Clip-ad: A language-guided staged dual-path model for zero-shot anomaly detection,” in *International Joint Conference on Artificial Intelligence*. Springer, 2024, pp. 17–33.

[10] Alexey Dosovitskiy, Lucas Beyer, Alexander Kolesnikov, Dirk Weissenborn, Xiaohua Zhai, Thomas Unterthiner, Mostafa Dehghani, Matthias Minderer, Georg Heigold, Sylvain Gelly, et al., “An image is worth 16x16 words: Transformers for image recognition at scale,” *arXiv preprint arXiv:2010.11929*, 2020.

[11] Jonathan Long, Evan Shelhamer, and Trevor Darrell, “Fully convolutional networks for semantic segmentation,” in *Proceedings of the IEEE conference on computer vision and pattern recognition*, 2015, pp. 3431–3440.

[12] Olaf Ronneberger, Philipp Fischer, and Thomas Brox, “U-net: Convolutional networks for biomedical image segmentation,” in *International Conference on Medical image computing and computer-assisted intervention*. Springer, 2015, pp. 234–241.

[13] Neil Houlsby, Andrei Giurgiu, Stanislaw Jastrzebski, Bruna Morrone, Quentin De Laroussilhe, Andrea Gesmundo, Mona Attariyan, and Sylvain Gelly, “Parameter-efficient transfer learning for nlp,” in *International conference on machine learning*. PMLR, 2019, pp. 2790–2799.

[14] Edward J Hu, Yelong Shen, Phillip Wallis, Zeyuan Allen-Zhu, Yuanzhi Li, Shean Wang, Lu Wang, Weizhu Chen, et al., “Lora: Low-rank adaptation of large language models,” *ICLR*, vol. 1, no. 2, pp. 3, 2022.

[15] Shibo Jie, Zhi-Hong Deng, Shixuan Chen, and Zhijuan Jin, “Convolutional bypasses are better vision transformer adapters,” in *ECAI 2024*, pp. 202–209. IOS Press, 2024.

[16] Zihan Zhong, Zhiqiang Tang, Tong He, Haoyang Fang, and Chun Yuan, “Convolution meets lora: Parameter efficient finetuning for segment anything model,” *arXiv preprint arXiv:2401.17868*, 2024.

[17] Tsung-Yi Lin, Priya Goyal, Ross Girshick, Kaiming He, and Piotr Dollár, “Focal loss for dense object detection,” in *Proceedings of the IEEE international conference on computer vision*, 2017, pp. 2980–2988.

[18] Fausto Milletari, Nassir Navab, and Seyed-Ahmad Ahmadi, “V-net: Fully convolutional neural networks for volumetric medical image segmentation,” in *2016 fourth international conference on 3D vision (3DV)*. Ieee, 2016, pp. 565–571.

[19] Paul Bergmann, Michael Fauser, David Sattlegger, and Carsten Steger, “Mvtac ad—a comprehensive real-world dataset for unsupervised anomaly detection,” in *Proceedings of the IEEE/CVF conference on computer vision and pattern recognition*, 2019, pp. 9592–9600.

[20] Yang Zou, Jongheon Jeong, Latha Pemula, Dongqing Zhang, and Onkar Dabeer, “Spot-the-difference self-supervised pre-training for anomaly detection and segmentation,” in *European conference on computer vision*. Springer, 2022, pp. 392–408.

[21] Pankaj Mishra, Riccardo Verk, Daniele Fornasier, Claudio Piciarelli, and Gian Luca Foresti, “Vt-adl: A vision transformer network for image anomaly detection and localization,” in *2021 IEEE 30th International Symposium on Industrial Electronics (ISIE)*. IEEE, 2021, pp. 01–06.

[22] Stepan Jezek, Martin Jonak, Radim Burget, Pavel Dvorak, and Milos Skotak, “Deep learning-based defect detection of metal parts: evaluating current methods in complex conditions,” in *2021 13th International congress on ultra modern telecommunications and control systems and workshops (ICUMT)*. IEEE, 2021, pp. 66–71.

[23] Haomin Yu, Qingyong Li, Yunqiang Tan, Jinrui Gan, Jianzhu Wang, Yangli-ao Geng, and Lei Jia, “A coarse-to-fine model for rail surface defect detection,” *IEEE Transactions on Instrumentation and Measurement*, vol. 68, no. 3, pp. 656–666, 2018.

[24] Jinan Bao, Hanshi Sun, Hanqiu Deng, Yinsheng He, Zhaoxiang Zhang, and Xingyu Li, “Bmad: Benchmarks for medical anomaly detection,” in *Proceedings of the IEEE/CVF Conference on Computer Vision and Pattern Recognition*, 2024, pp. 4042–4053.

[25] Nima Tajbakhsh, Suryakanth R Gurudu, and Jianming Liang, “Automated polyp detection in colonoscopy videos using shape and context information,” *IEEE transactions on medical imaging*, vol. 35, no. 2, pp. 630–644, 2015.

[26] Jorge Bernal, F Javier Sánchez, Gloria Fernández-Esparrach, Debora Gil, Cristina Rodríguez, and Fernando Vilariño, “Wmdova maps for accurate polyp highlighting in colonoscopy: Validation vs. saliency maps from physicians,” *Computerized medical imaging and graphics*, vol. 43, pp. 99–111, 2015.

[27] Debesh Jha, Pia H Smedsrød, Michael A Riegler, Pål Halvorsen, Thomas De Lange, Dag Johansen, and Håvard D Johansen, “Kvasir-seg: A segmented polyp dataset,” in *International conference on multimedia modeling*. Springer, 2019, pp. 451–462.